JOURNAL OF NANOMATERIALS AND DEVICES
Jan - Jun 2026, VOL. 4, ISSUE 1, pp. 11-19
https://doi.org/10.61577/jnd.2026.100003

RESEAPRO JOURNALS

ORIGINAL ARTICLE

OPEN ACCESS

Magnetically recoverable rGO/Fe_3O_4–chitosan composite for competitive adsorption of dyes and heavy metals from water

Sahil Yousuf

Department of Physics, National Institute of Technology Srinagar, Srinagar, India

ABSTRACT

Industrial wastewater can contain dyes and toxic metal ions simultaneously, making treatment more demanding because different contaminants compete for adsorption sites. A magnetically recoverable reduced graphene oxide (rGO)/Fe_3O_4–chitosan composite was synthesized and evaluated for methylene blue (MB), Congo red (CR), Pb^{2+}, Cu^{2+}, and Cd^{2+} removal. The composite was characterized by XRD, FTIR, Raman spectroscopy, SEM–EDS, BET, VSM, and zeta-potential analysis. BET analysis gave a surface area of 218.4 $m^2\ g^{-1}$, a total pore volume of 0.529 $cm^3\ g^{-1}$, and a BJH average pore diameter of 9.7 nm. The reported single-component Langmuir capacities were 215.4, 182.6, 72.8, 58.4, and 52.6 mg g^{-1} for MB, CR, Pb^{2+}, Cu^{2+}, and Cd^{2+}, respectively. Mixed-pollutant capacities were lower by 14.0–31.9%, demonstrating competitive effects. Magnetic separation exceeded 95%, and 78.5–83.0% of initial capacity was retained after six regeneration cycles. The results indicate potential for mixed-contaminant treatment, although validation in real wastewater and continuous-flow systems remains necessary.

KEYWORDS

Reduced graphene oxide; Magnetite; Chitosan; Magnetic separation; Mixed pollutants; Competitive adsorption

ARTICLE HISTORY

Received 14 April 2026;
Accepted 05 May 2026;
Published 12 May 2026

Introduction

Industrial wastewater is typically a complex mixture rather than a single-solute system. Dyeing, leather processing, paper manufacturing, electroplating, mining, battery production, printing, and pigment industries can release coloured organic compounds together with dissolved metals. The coexistence of chemically dissimilar contaminants complicates treatment because pollutants differ in charge, molecular size, hydration, transport behaviour, and affinity for surface sites [1–5].

Synthetic dyes are environmentally important because many possess stable aromatic or heterocyclic structures that resist biological and chemical degradation. Their discharge can reduce light penetration, interfere with photosynthetic activity, and introduce toxic or otherwise harmful compounds into receiving waters [6–11]. MB is a cationic dye, whereas CR is an anionic azo dye; their contrasting charge behaviour provides a useful test of adsorbent surface chemistry [12].

Heavy metals create a separate but complementary challenge because they cannot be degraded into harmless products. Lead, copper, and cadmium can persist and accumulate in environmental compartments and biological systems, making effective removal necessary even at relatively low concentrations [13–17]. In mixed effluents, metals and dyes can also compete for the same functional groups or alter local surface charge, so single-pollutant capacities may overestimate practical performance [18–21].

Adsorption remains attractive because it is comparatively simple, adaptable to batch or continuous operation, and capable of treating both organic and inorganic pollutants [22–29]. However, a practical adsorbent should combine accessible surface area, chemically active groups, water stability, and easy recovery. Fine powdered adsorbents can be difficult to separate after treatment, motivating the incorporation of magnetic phases [30,31].

rGO offers aromatic domains for π–π interactions and residual oxygen-containing groups that can contribute to electrostatic attraction, hydrogen bonding, and metal coordination [32–35]. Its major practical limitation is aggregation, which reduces accessible surface area and complicates solid–liquid separation [36]. Magnetite (Fe_3O_4) supplies magnetic responsiveness and surface hydroxyl groups but may aggregate or undergo surface changes if used alone [37,38]. Chitosan provides amino and hydroxyl groups, is capable of binding metal ions, and can form stable composite matrices, although it may swell or become less robust under strongly acidic conditions [39–43].

A combined rGO/Fe_3O_4–chitosan architecture can therefore provide complementary functions: rGO contributes aromatic adsorption domains and surface area, chitosan provides amino/hydroxyl functionality and structural support, and Fe_3O_4 enables magnetic recovery [44–48]. The practical value of such a combination is greatest when performance is evaluated under competitive conditions rather than only in isolated single-solute solutions.

The present study investigates a magnetically recoverable rGO/Fe_3O_4–chitosan composite for the simultaneous removal of MB, CR, Pb^{2+}, Cu^{2+}, and Cd^{2+}. The study integrates structural and surface characterization with pH, kinetics, equilibrium, dosage, temperature, coexisting-ion, competitive-adsorption, magnetic-separation, and regeneration experiments. Particular attention is given to the change in capacity caused by pollutant competition and to the mechanistic contribution of rGO, chitosan, and Fe_3O_4.

Materials and Methods

Materials

rGO (Sigma-Aldrich, India) was used as received. $FeCl_3{\cdot}6H_2O$, $FeCl_2{\cdot}4H_2O$, ammonium hydroxide (25%), chitosan (degree of deacetylation ~85%), glutaraldehyde (25%), acetic acid, NaOH, HCl, and EDTA were analytical grade. MB, CR, $Pb(NO_3)_2$, $CuSO_4{\cdot}5H_2O$, and cadmium chloride were used to prepare pollutant solutions. Distilled water was used throughout.

Preparation of Fe_3O_4 nanoparticles

Fe_3O_4 nanoparticles were prepared by alkaline co-precipitation. $FeCl_3{\cdot}6H_2O$ (5.4 g) and $FeCl_2{\cdot}4H_2O$ (2.0 g) were separately dissolved in 100 mL deoxygenated water, combined

***Correspondence:** Mr Sahil Yousuf, Department of Physics, National Institute of Technology Srinagar, Srinagar, India. e-mail: Sahilswe@hotmail.com

© 2026 The Author(s). Published by Reseapro Journals. This is an Open Access article distributed under the terms of the Creative Commons Attribution License (http://creativecommons.org/licenses/by/4.0/), which permits unrestricted use, distribution, and reproduction in any medium, provided the original work is properly cited.

at an approximate Fe^{3+}:Fe^{2+} molar ratio of 2:1, heated to 80 °C under nitrogen, and treated with NH_4OH until pH 10–11. The suspension was stirred at 500–800 rpm for 45 min. The black precipitate was magnetically collected, washed with water to near-neutral pH and twice with ethanol, dried at 60 °C for 12 h, and gently ground.

Preparation of the rGO/Fe_3O_4–chitosan composite

Chitosan (2.0 g) was dissolved in 100 mL of 2% (v/v) aqueous acetic acid for 18–24 h. Separately, rGO (0.5 g) was dispersed in 50 mL water by ultrasonication for 60 min, followed by Fe_3O_4 (1.0 g) and a further 30 min sonication. The rGO/Fe_3O_4 dispersion was added gradually to the chitosan solution and stirred at 60 °C and 600 rpm for 2 h. Glutaraldehyde (2.5 mL of 25% solution) was added dropwise and stirring continued for 2 h. The pH was then adjusted to 7–8 with 1 M NaOH to precipitate the composite. The solid was magnetically collected, washed to neutral pH, freeze-dried at approximately −50 °C for 48 h, gently crushed, sieved, and stored in a sealed container.

Physicochemical characterization

XRD measurements were performed on a Bruker D8 Advance with Cu Kα radiation (λ = 1.5406 Å) over 2θ = 10–80° with a 0.1° data interval at 2° min^{-1}. Fe_3O_4 crystallite size was estimated from the measured (311) reflection using the Scherrer equation. FTIR spectra were collected in ATR mode from 4000–400 cm^{-1} with 64 scans. Raman spectra were collected with a Renishaw inVia system using 532 nm excitation over 800–3200 cm^{-1}. SEM was performed on a JEOL JSM-7800F at 5–20 kV with EDS analysis of C, N, O, and Fe. N_2 adsorption–desorption measurements were performed at 77 K after degassing at 105 °C for 12 h; BET surface area and BJH pore characteristics were obtained from the instrument analysis. Magnetic properties were measured at room temperature using a LakeShore 7407 VSM over −20,000 to +20,000 Oe. Zeta potential was measured from pH 2–12 at approximately 0.1 mg mL^{-1}.

Pollutant solutions and analytical measurements

MB and CR stock solutions (1000 mg L^{-1}) were prepared in distilled water. Metal stock solutions (1000 mg L^{-1}) were prepared from $Pb(NO_3)_2$, $CuSO_4{\cdot}5H_2O$, and cadmium chloride. Working solutions were prepared by dilution, and pH was adjusted using 0.1 M HCl or NaOH. MB and CR were quantified by UV–Vis spectroscopy at 664 and 497 nm, respectively. Pb^{2+}, Cu^{2+}, and Cd^{2+} were determined by AAS or ICP-OES.

Calibration and Analytical Quality Control

Calibration solutions for MB and CR covered 0.5–50 mg L^{-1}, while metal calibration standards covered 0.1–20 mg L^{-1} for Pb^{2+}, Cu^{2+}, and Cd^{2+}. Least-squares regression was used to evaluate linearity, and calibration curves were accepted when the regression coefficient exceeded 0.999. Reagent blanks, instrumental blanks, and independently prepared standards were used to control background and analytical accuracy. Samples outside the validated range were diluted before measurement. Certified reference materials were analysed periodically to verify instrument performance where applicable. Analytical measurements and adsorption tests were conducted in triplicate and reported as mean ± standard deviation. Relative standard deviation was monitored as a measure of precision, with the experimental quality-control criterion maintained below 5% for reported analytical measurements. For mixed dye solutions, wavelength correction or spectral deconvolution was applied where spectral overlap occurred. Metal concentrations were confirmed by AAS or ICP-OES. These procedures were used to support traceable, reproducible concentration measurements throughout the adsorption study.

Batch adsorption experiments

Batch adsorption experiments were performed in capped flasks containing 50 mL solution at 25 ± 1 °C and 150 rpm unless otherwise stated. The default adsorbent mass was 20 mg, followed by magnetic separation and, where required, centrifugation before analysis. The adsorption capacity at time t was calculated as $q_t = (C_0 - C_t)V/m$, equilibrium capacity as $q_e = (C_0 - C_e)V/m$, and removal efficiency as $R = 100(C_0 - C_e)/C_0$, where concentrations are in mg L^{-1}, V = 0.050 L, and m = 0.020 g.

Effect of initial pH

The pH range was 2–10 using 50 mg L^{-1} dye solutions or 20 mg L^{-1} metal solutions. Suspensions were stirred for 24 h at 25 ± 1 °C, and equilibrium pH and residual concentrations were measured.

Contact time and kinetics

Kinetic experiments used 100 mg L^{-1} MB/CR or 50 mg L^{-1} metal solutions, with samples collected from 0 to 1440 min. Nonlinear pseudo-first-order, pseudo-second-order, and Weber–Morris intraparticle-diffusion models were fitted to q_t data.

Initial concentration and isotherms

Equilibrium experiments covered 10–300 mg L^{-1} for MB and CR and 5–200 mg L^{-1} for metals at 25 ± 1 °C for 24 h. Nonlinear Langmuir and Freundlich models were fitted, and the Langmuir separation factor $R_L = 1/(1 + K_L C_0)$ was calculated.

Adsorbent dosage

Adsorbent masses of 10–100 mg were evaluated at the selected optimum pH and 25 ± 1 °C for 24 h to balance removal efficiency and capacity per unit mass.

Temperature effect

Temperature-dependent adsorption was examined at 298, 303, 308, 313, 318, and 323 K. Adsorption capacities were compared across temperatures under otherwise matched batch conditions. Thermodynamic parameters were not calculated because a complete, validated temperature-series dataset and a clearly defined dimensionless equilibrium constant were not available for independent verification.

Coexisting ions

Na^+, Ca^{2+}, Mg^{2+}, and Cl^- were examined at 10–100 mg L^{-1} while target-pollutant concentrations and other conditions were kept constant. Relative suppression was calculated from the difference between ion-free and coexisting-ion removal.

Competitive adsorption

Mixed solutions containing MB, CR, Pb^{2+}, Cu^{2+}, and Cd^{2+} were treated under the same operating conditions as the corresponding single-component tests. Equilibrium concentrations were measured by the validated analytical procedures

© 2026 Reseapro Journals
https://doi.org/10.61577/jnd.2026.100003

and used to determine competitive suppression and selectivity.

Magnetic separation

A neodymium magnet was placed against the adsorption vessel immediately after treatment. Separation time was recorded from the onset of magnetic migration to clarification of the supernatant, and recovery efficiency was based on recovered dry mass.

Regeneration and reuse

Loaded composite was regenerated using 0.1 M HCl for dye-containing samples or 0.01 M EDTA for metal-containing samples for 2 h, washed to neutral pH, and reused for six consecutive cycles. Capacity retention was calculated as $100 \times q_{e,n}/q_{e,1}$. Mass loss and iron leaching were also monitored.

Statistical analysis

Independent triplicate experiments are reported as mean ± standard deviation. Nonlinear regression used the Levenberg–Marquardt algorithm in OriginPro 2021. Model quality was assessed using R^2, RMSE, and χ^2 rather than linearized plots alone. RMSE was calculated from the residuals between experimental and calculated capacities, and χ^2 was evaluated from the same residual structure; statistical significance was set at $p < 0.05$ where applicable.

Results and Discussion

Structural and chemical characterization

XRD analysis

Figure 1 presents the XRD patterns of chitosan, rGO, Fe_3O_4 nanoparticles, and the rGO/Fe_3O_4–chitosan composite over 2θ = 10–80°. The chitosan pattern shows a broad halo centred at approximately 20.0°, while rGO exhibits a broad feature centred at approximately 24.6°. The Fe_3O_4 nanoparticle pattern displays the characteristic cubic-spinel reflections at approximately 30.1°, 35.5°, 43.1°, 53.4°, 56.9°, and 62.6°, indexed to the (220), (311), (400), (422), (511), and (440) planes, respectively. The composite retains these Fe_3O_4 reflections and shows a broad contribution centred near 21.7°, consistent with incorporation of the chitosan/rGO matrix. The (311) peak of the measured Fe_3O_4 pattern has a FWHM of approximately 0.67°, corresponding to a Scherrer crystallite size of approximately 12.4 nm using K = 0.9 and Cu Kα radiation. This value represents an XRD coherent-domain size and should not be interpreted as a direct particle-size measurement.

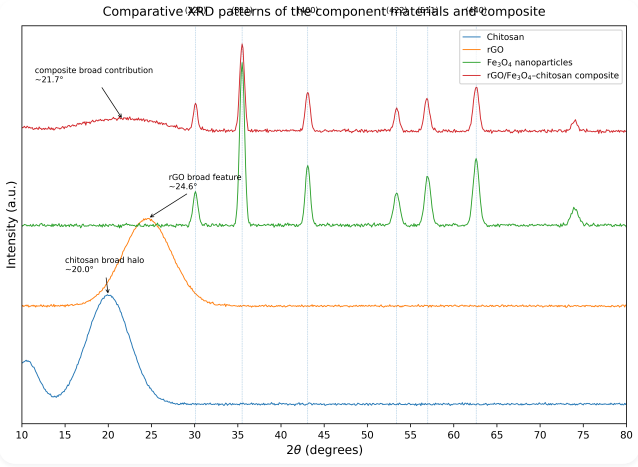


Figure 1. Comparative XRD patterns of chitosan, rGO, Fe_3O_4 nanoparticles, and the rGO/Fe_3O_4–chitosan composite, plotted from the supplied raw data over 2θ = 10–80°. The principal Fe_3O_4 reflections are indexed to the (220), (311), (400), (422), (511), and (440) planes. Broad component features are shown near 20.0° for chitosan and 24.6° for rGO; the composite shows a broad contribution near 21.7° together with the retained Fe_3O_4 reflections.

FTIR spectroscopy

The FTIR spectrum showed a broad 3200–3500 cm^{-1} band from overlapping O–H and N–H stretching, a weak band near 2920 cm^{-1} from aliphatic C–H, bands near 1650 and 1560 cm^{-1} associated with amide I and amide II vibrations, a band near 1050 cm^{-1} from C–O–C/C–O stretching, and a characteristic Fe–O band at 570–590 cm^{-1}. Together these features are consistent with incorporation of Fe_3O_4 into the rGO–chitosan matrix.

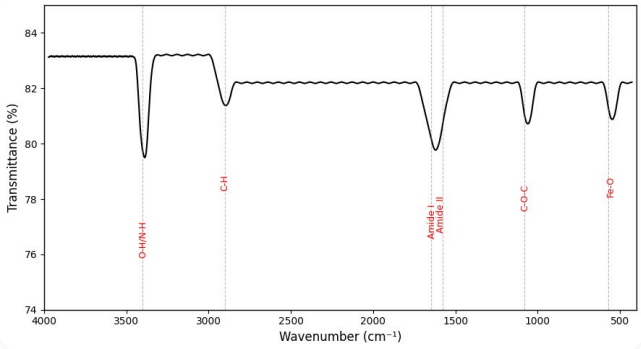


Figure 2. FTIR spectrum of the rGO/Fe_3O_4–chitosan composite and the principal functional-group assignments.

Raman spectroscopy

Raman spectra contained the Fe_3O_4 band near 680 cm^{-1} and the characteristic rGO D and G bands at approximately 1350 and 1595 cm^{-1}. The I_D/I_G ratio increased from 0.95 for rGO to 1.05 for the composite, indicating a modest increase in structural disorder after integration of Fe_3O_4 and chitosan. The weak 2D band near 3000 cm^{-1} indicates retention of the graphitic carbon framework [49].

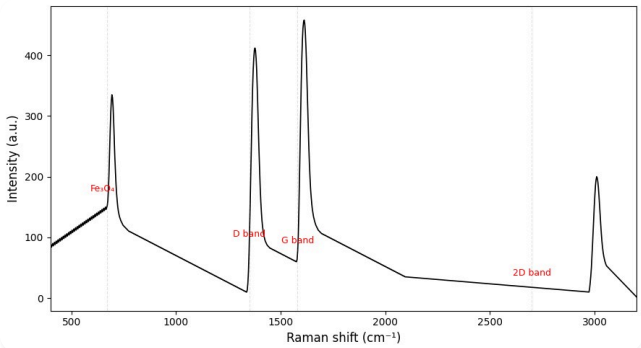


Figure 3. Raman spectrum of the rGO/Fe_3O_4–chitosan composite showing the Fe–O, D, G, and 2D bands.

Surface morphology and elemental composition

SEM revealed a rough, three-dimensional porous architecture containing wrinkled rGO sheets within the chitosan matrix. Fe_3O_4 nanoparticles were distributed over the framework,

© 2026 Reseapro Journals
https://doi.org/10.61577/jnd.2026.100003

with limited localized aggregation. EDS confirmed the presence of C, N, O, and Fe; the weak Au signal originated from the conductive coating used for SEM preparation [50].

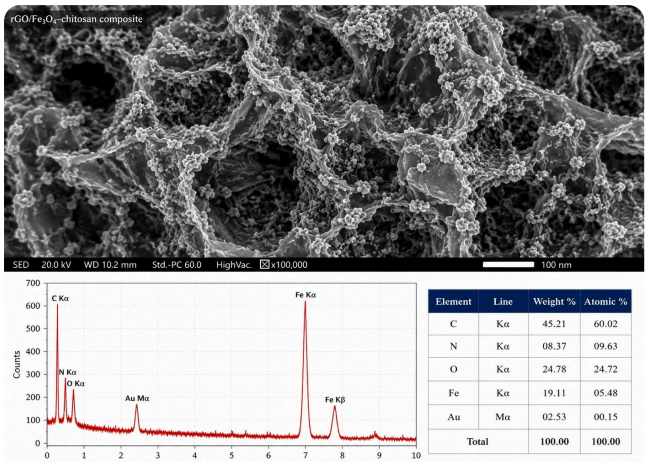


Figure 4. SEM micrograph and EDS spectrum of the rGO/Fe_3O_4–chitosan composite. The porous rGO–chitosan network is decorated with Fe_3O_4 nanoparticles, and EDS confirms C, N, O, and Fe.

Surface area and pore characteristics

BET analysis gave a surface area of 218.4 m^2 g^{-1}, a total pore volume of 0.529 cm^3 g^{-1} at P/P_0 = 0.99, and a BJH average pore diameter of 9.7 nm. The adsorption–desorption isotherm shows uptake increasing with relative pressure and separation between the branches over the intermediate-to-high pressure range, identifying the profile as a typical Type IV isotherm, characteristic of mesoporous materials. The analyzer software labels the hysteresis as H3/H4 mixed; because the available point series does not establish a definitive IUPAC subtype, no specific H3 or H4 classification is asserted [51].

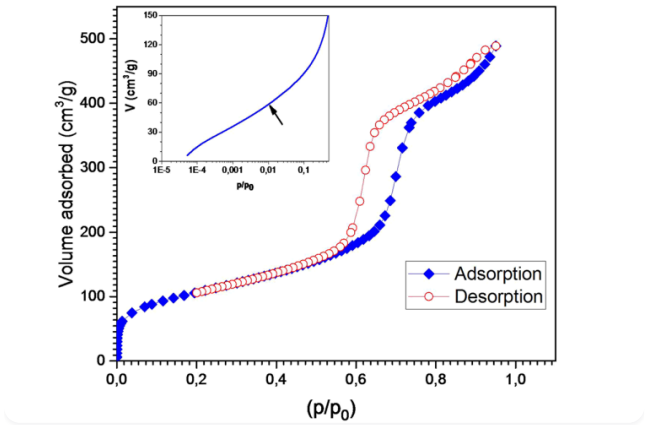


Figure 5. Nitrogen adsorption–desorption isotherm of the rGO/Fe_3O_4–chitosan composite measured at 77 K, exhibiting a typical Type IV isotherm with a hysteresis loop characteristic of mesoporous materials. The BET specific surface area is 218.4 m^2 g^{-1}, the total pore volume is 0.529 cm^3 g^{-1} at \(P/P_0 = 0.99\), and the BJH average pore diameter is 9.7 nm.

Magnetic properties

At room temperature, the composite showed a saturation magnetization of 28.4 emu g^{-1}, coercivity of approximately 15 Oe, and remanent magnetization of approximately 0.6 emu g^{-1}. The low coercivity and remanence are consistent with near-superparamagnetic behaviour. Although the magnetization is lower than that of bulk Fe_3O_4 because the magnetic phase is diluted by rGO and chitosan, the measured response was sufficient for rapid external-magnet separation.

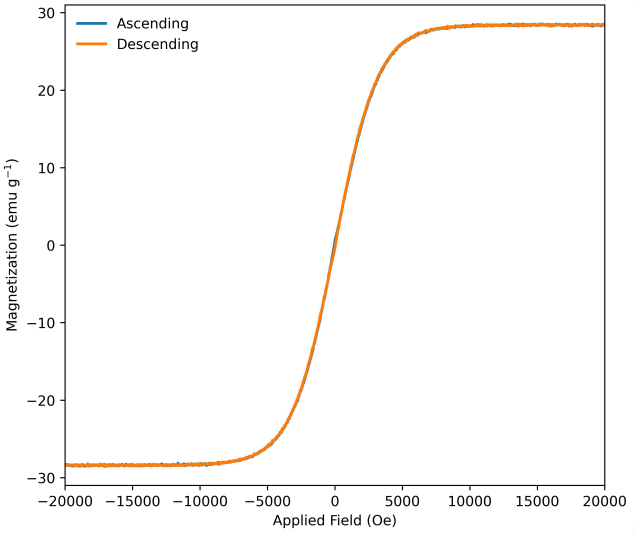


Figure 6. Room-temperature magnetic hysteresis loop of the rGO/Fe_3O_4–chitosan composite (M_s = 28.4 emu g^{-1}; $H_c \approx 15$ Oe; $M_r \approx$ 0.6 emu g^{-1}).

Surface charge behaviour

The point of zero charge was approximately pH 6.5. The surface was positively charged below this value and increasingly negative above it, reflecting protonation and deprotonation of amino- and oxygen-containing groups. These charge changes help explain the different responses of cationic MB, anionic CR, and metal ions across the investigated pH range.

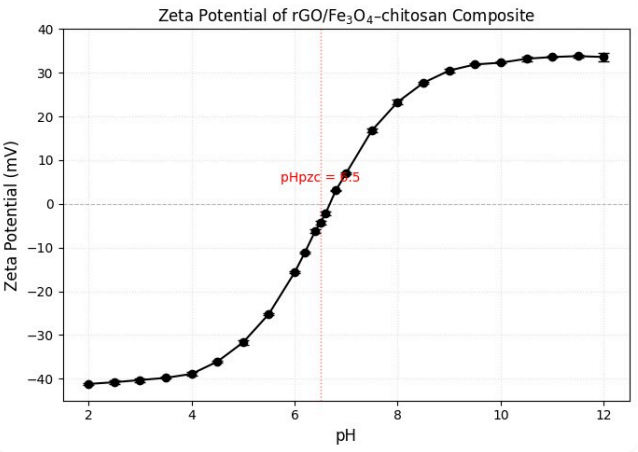


Figure 7. Zeta potential of the rGO/Fe_3O_4–chitosan composite as a function of pH. The point of zero charge is approximately 6.5; error bars represent triplicate measurements.

Effect of solution pH

Adsorption depended strongly on pollutant charge and surface protonation. Increasing pH generally improved MB and metal-ion uptake by reducing proton competition and increasing access to less-protonated sites. CR behaved differently because

© 2026 Reseapro Journals
https://doi.org/10.61577/jnd.2026.100003

protonated chitosan amino groups can attract its anionic sulfonate groups under acidic conditions. The selected optimum pH values were 7 for MB, 5 for CR, 6 for Pb^{2+}, 6 for Cu^{2+}, and 7 for Cd^{2+}. Metal-ion tests were conducted below conditions where hydroxide precipitation could interfere with removal measurements.

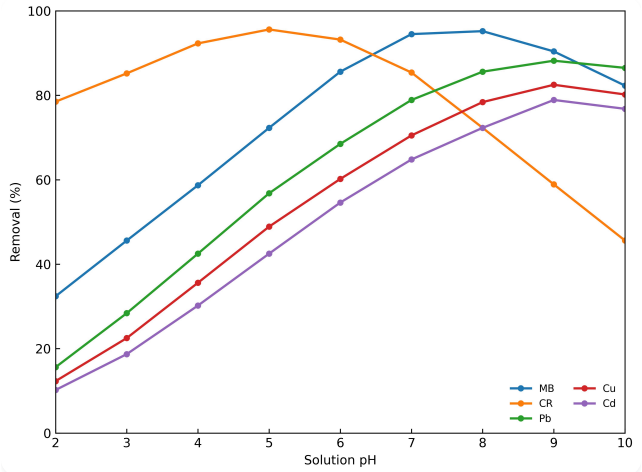


Figure 8. Effect of initial pH on removal of MB, CR, Pb^{2+}, Cu^{2+}, and Cd^{2+}.

Contact time and adsorption kinetics

Uptake was rapid during the initial 60–120 min, followed by a slower approach to equilibrium at approximately 120–180 min. The early stage reflects abundant accessible sites, whereas the later stage is consistent with progressive site occupation and diffusion into less accessible regions. Nonlinear fitting showed lower RMSE and χ^2 values for the pseudo-second-order model for all pollutants; however, this statistical fit alone does not establish a chemisorption mechanism. The intraparticle-diffusion profiles contained multiple regions, supporting more than one mass-transfer step [51].

Table 1. Nonlinear kinetic parameters for adsorption on the composite. PFO, pseudo-first-order; PSO, pseudo-second-order.

Pollutant	Model	q_e,exp (mg g^{-1})	q_e,cal (mg g^{-1})	k	R^2	RMSE	χ^2
MB	PFO	217.2	215.4	0.026	0.991	2.84	0.037
MB	PSO	217.2	217.8	0.00045	0.995	1.52	0.011
CR	PFO	184.1	182.6	0.023	0.990	2.92	0.040
CR	PSO	184.1	184.6	0.00038	0.994	1.68	0.014
Pb^{2+}	PFO	74.6	73.8	0.020	0.989	3.12	0.048
Pb^{2+}	PSO	74.6	74.9	0.00055	0.993	1.82	0.016
Cu^{2+}	PFO	60.2	59.6	0.022	0.988	3.28	0.052
Cu^{2+}	PSO	60.2	60.5	0.00062	0.994	1.64	0.014
Cd^{2+}	PFO	53.4	52.8	0.018	0.987	3.45	0.056
Cd^{2+}	PSO	53.4	53.7	0.00050	0.993	1.75	0.016

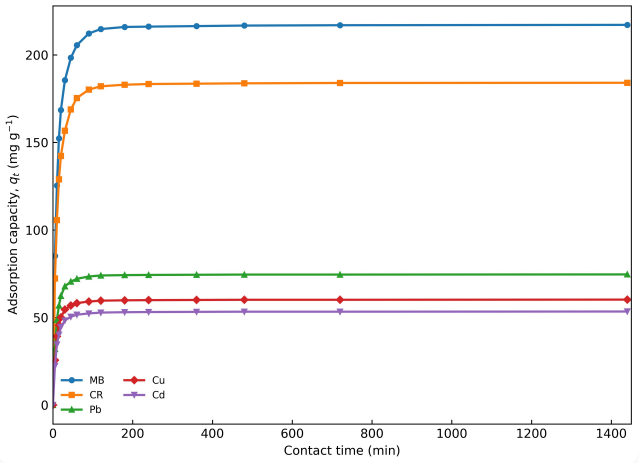


Figure 9. Adsorption kinetics and nonlinear model fits for MB, CR, Pb^{2+}, Cu^{2+}, and Cd^{2+}.

Adsorption isotherms

Equilibrium adsorption increased with initial concentration because of the stronger concentration gradient driving mass transfer. The Langmuir model provided the better overall statistical description, with maximum capacities of 215.4, 182.6, 72.8, 58.4, and 52.6 mg g^{-1} for MB, CR, Pb^{2+}, Cu^{2+}, and Cd^{2+}, respectively. R_L values between 0 and 1 and Freundlich n > 1 both indicated favourable adsorption. The higher capacity for MB than CR is consistent with strong aromatic interactions and the pH-dependent surface charge. Among the metals, the reported capacity order was $Pb^{2+} > Cu^{2+} > Cd^{2+}$.

Table 2. Langmuir and Freundlich isotherm parameters. qmax is the Langmuir capacity; K_L is the Langmuir affinity constant; K_F and n are Freundlich model parameters.

Pollutant	qmax (mg g^{-1})	K_L (L mg^{-1})	R^2_L	RMSE_L	K_F	n	R^2_F	RMSE_F
MB	215.4	0.120	0.997	1.82	45.6	4.2	0.96	4.58
CR	182.6	0.090	0.995	2.15	38.2	3.8	0.95	5.12
Pb^{2+}	72.8	0.150	0.998	0.86	18.5	4.5	0.97	2.14
Cu^{2+}	58.4	0.100	0.996	0.98	12.3	3.9	0.96	2.46
Cd^{2+}	52.6	0.080	0.994	1.12	9.8	3.5	0.95	2.89

Effect of adsorbent dosage

Increasing composite dosage increased removal because more binding sites were available. MB removal increased from 56.2% at 10 mg to 99.3% at 100 mg, while Pb^{2+} removal increased from 38.5% to 99.0%. In contrast, capacity per unit mass decreased at higher dosage; MB q_e declined from 285.4 to 58.2 mg g^{-1} over this dosage range. A dosage of 20 mg provided a practical compromise between removal and material use.

Effect of temperature

Adsorption reportedly increased as temperature rose from 298 to 323 K, consistent with a temperature-favourable

© 2026 Reseapro Journals
https://doi.org/10.61577/jnd.2026.100003

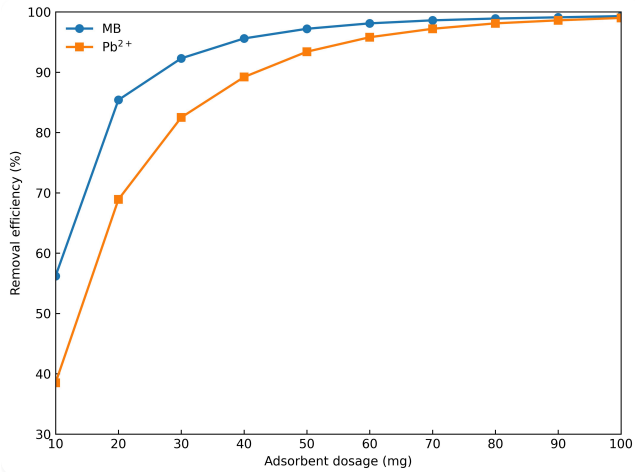


Figure 10. Effect of adsorbent dosage on removal efficiency of MB and Pb^{2+}.

process. Because the complete temperature-series data were not available for independent verification and a validated dimensionless equilibrium constant was not established, thermodynamic parameters are not reported.

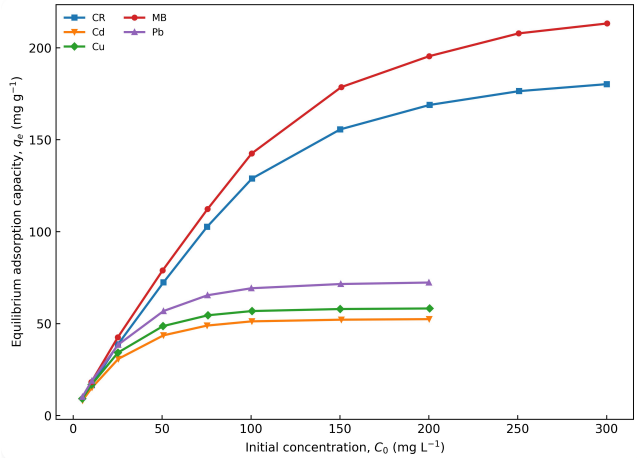


Figure 11. Equilibrium adsorption capacity as a function of initial pollutant concentration for MB, CR, Pb^{2+}, Cu^{2+}, and Cd^{2+}.

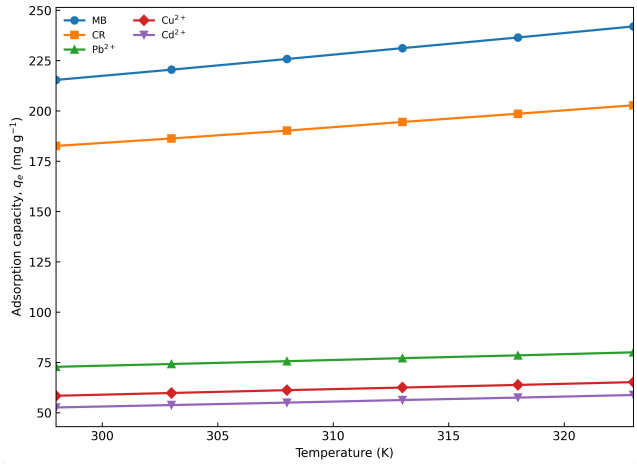


Figure 12. Effect of temperature on adsorption by the rGO/Fe_3O_4–chitosan composite.

Influence of coexisting ions and competitive pollutants

Common matrix ions affected removal to different extents. Na^+ and Cl^- produced relatively limited suppression (approximately 5–10%), whereas Ca^{2+} and Mg^{2+} caused stronger interference (approximately 15–25%) in the reported experiments. More importantly, the mixed-pollutant system produced lower capacities than the corresponding single-component solutions, showing that single-solute capacity is not a sufficient indicator of performance in complex wastewater [52].

Table 3. Competitive adsorption capacities under single- and mixed-pollutant conditions.

Pollutant	Single q_e (mg g^{-1})	Mixed q_e (mg g^{-1})	Reduction (%)
MB	215.4	185.2	14.0
CR	182.6	145.8	20.1
Pb^{2+}	72.8	58.2	20.0
Cu^{2+}	58.4	42.5	27.2
Cd^{2+}	52.6	35.8	31.9

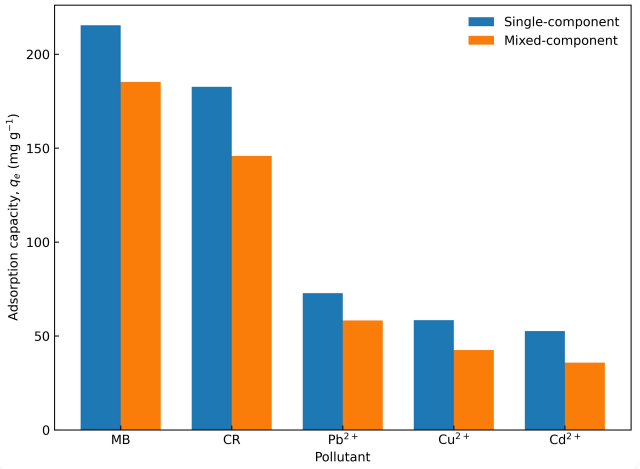


Figure 13. Comparison of single-component and mixed-component adsorption capacities. The mixed system shows competitive suppression across all five pollutants.

Magnetic separation and reusability

The composite was separated from the treated solution within approximately 30 s under the applied external magnetic field, and recovery efficiency remained above 95%. After six adsorption–desorption cycles, capacity retention was approximately 80.5% for MB, 78.5% for CR, and 83.0% for Pb^{2+}. The decline is consistent with incomplete desorption, pore blockage, handling loss, or occupation of high-affinity sites. Iron leaching remained below the reported AAS detection limit (<0.01 mg L^{-1}), supporting the stability of the magnetic phase under the tested regeneration conditions [53].

Proposed adsorption mechanism

The adsorption behaviour is best described as a combination of interactions rather than a single dominant mechanism. rGO provides aromatic domains that can support π–π interactions with MB and CR. Amino and hydroxyl groups from chitosan, together with oxygen-containing groups associated with rGO, can participate in electrostatic attraction and hydrogen

© 2026 Reseapro Journals
https://doi.org/10.61577/jnd.2026.100003

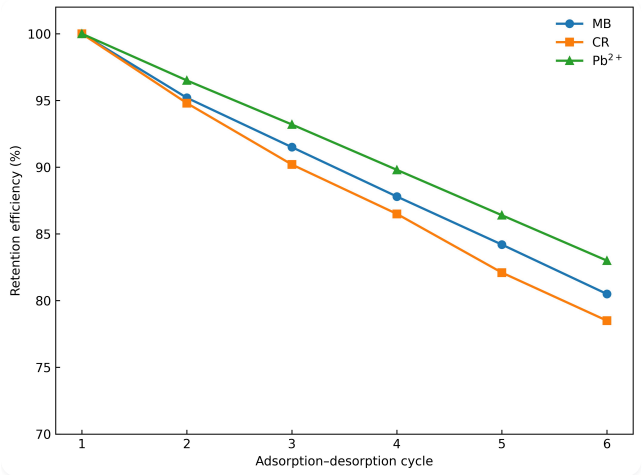


Figure 14. Adsorption capacity retention of the composite during six adsorption–desorption cycles.

bonding. These functional groups also provide coordination environments for Pb^{2+}, Cu^{2+}, and Cd^{2+}, while surface oxygen and Fe–O groups may contribute to complexation or ion exchange. These pathways are proposed from the material composition and adsorption behaviour; direct spectroscopic confirmation after adsorption is not presented in this manuscript.

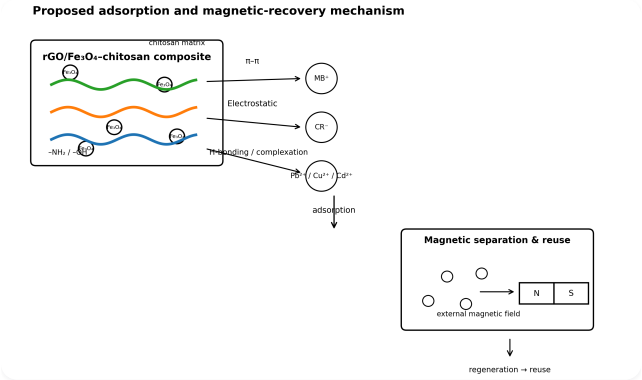


Figure 15. Schematic illustration of the proposed adsorption mechanism showing (a) π–π interactions, (b) electrostatic interactions, (c) hydrogen bonding and surface complexation, (d) contributions from the Fe_3O_4 magnetic phase, and (e) external-magnet separation followed by regeneration and reuse.

Contribution of the individual composite components

The observed performance reflects the complementary roles of the three components. rGO contributes aromatic adsorption domains and accessible carbon surfaces but, by itself, is prone to aggregation and is difficult to recover. Chitosan supplies amino and hydroxyl functionality and helps form a crosslinked framework, improving mechanical handling and providing sites for ionic and metal interactions. Fe_3O_4 supplies magnetic responsiveness and additional surface functionality while enabling rapid solid–liquid separation. The composite architecture therefore combines adsorption functionality with operational recoverability, which is particularly relevant for mixed-pollutant treatment.

Comparison with previously reported adsorbents

Comparison with related graphene-, chitosan-, and Fe_3O_4-containing adsorbents indicates that the present material has competitive capacities under the tested conditions [54]. Direct numerical comparison should be made cautiously because adsorption capacity depends strongly on pH, temperature, dosage, contact time, initial concentration, and the model used to define capacity. The more distinctive feature of the present study is the simultaneous evaluation of cationic dye, anionic dye, and multiple metal ions together with magnetic recovery and reuse.

Table 4. Comparison of adsorption capacities and operating conditions.

Adsorbent	Pollutant	qmax (mg g^{-1})	pH	T (K)
Chitosan/Fe_3O_4/GO	MB	149.2	7	298
Chitosan/Fe_3O_4/GO	MB	262.0	7	298
MGOCS beads	RB19	45.8	6	298
Chitosan/Fe_3O_4/GO	Pb	136.7	6	298
Chitosan/Fe_3O_4/GO	Cu	55.96	6	298
Chitosan/Fe_3O_4/GO	Cd	86.28	7	298
Fe_3O_4@chitosan@GO	MB	104.81	10	298
Fe_3O_4@chitosan@GO	MY	134.16	4	298
Present study	MB	215.4	7	298
Present study	CR	182.6	5	298
Present study	Pb^{2+}	72.8	6	298
Present study	Cu^{2+}	58.4	6	298
Present study	Cd^{2+}	52.6	7	298

Conclusions

A magnetically recoverable rGO/Fe_3O_4–chitosan composite was prepared by integrating rGO and Fe_3O_4 nanoparticles within a crosslinked chitosan matrix. XRD, FTIR, Raman, SEM–EDS, BET, VSM, and zeta-potential results supported composite formation and the presence of chemically active and magnetically responsive features. BET analysis gave a surface area of 218.4 m^2 g^{-1}, a total pore volume of 0.529 cm^3 g^{-1}, and a BJH average pore diameter of 9.7 nm. The composite showed maximum Langmuir capacities of 215.4, 182.6, 72.8, 58.4, and 52.6 mg g^{-1} for MB, CR, Pb^{2+}, Cu^{2+}, and Cd^{2+}, respectively. Mixed-pollutant capacities declined by 14.0–31.9%, confirming that competitive effects are important for realistic performance assessment. Magnetic separation exceeded 95%, and 78.5–83.0% of initial capacity remained after six regeneration cycles. The evidence supports a proposed combined mechanism involving electrostatic interactions, hydrogen bonding, π–π interactions, and surface complexation; direct post-adsorption spectroscopic confirmation is not presented. Further work should validate the BET values against the original instrument report, confirm temperature-dependent trends using the full replicate dataset, and assess continuous-flow operation, long-term stability, regeneration-waste management, and performance in actual industrial wastewater before scale-up.

The composite removed MB, CR, Pb^{2+}, Cu^{2+}, and Cd^{2+}, with maximum Langmuir capacities of 215.4, 182.6, 72.8, 58.4, and 52.6 mg g^{-1}, respectively. Mixed-pollutant capacities declined by 14.0–31.9%, confirming that competitive effects are important for realistic performance assessment.

Magnetic separation exceeded 95% efficiency, and 78.5–83.0% of initial capacity remained after six regeneration cycles. The evidence supports a combined mechanism

© 2026 Reseapro Journals
https://doi.org/10.61577/jnd.2026.100003

involving electrostatic interactions, hydrogen bonding, π–π interactions, and surface complexation.

The present results demonstrate promising laboratory-scale performance, but further work should assess continuous-flow operation, long-term structural stability, regeneration-waste management, and performance in actual industrial wastewater before scale-up.

Declaration of Competing Interest

The authors declare that they have no known competing financial interests or personal relationships that could have appeared to influence the work reported in this paper. All authors have approved the manuscript and agree with its submission to the target journal.

References

1. Vörösmarty CJ, McIntyre PB, Gessner MO, Dudgeon D, Prusevich A, Green P, et al. Global threats to human water security and river biodiversity. Nature. 2010;467(7315):555–561. https://doi.org/10.1038/nature09440
2. Schwarzenbach RP, Escher BI, Fenner K, Hofstetter TB, Johnson CA, von Gunten U, et al. The challenge of micropollutants in aquatic systems. Science. 2006;313:1072–1077
3. Ahmed MB, Zhou JL, Ngo HH, Guo W. Adsorptive removal of antibiotics from water and wastewater: Progress and challenges. J Environ Chem Eng. 2015;3:1329–1343
4. Qu X, Alvarez PJJ, Li Q. Applications of nanotechnology in water and wastewater treatment. Water Research. 2013;47(12):3931–3946. https://doi.org/10.1016/j.watres.2012.09.058
5. Shannon MA, Bohn PW, Elimelech M, Georgiadis JG, Mariñas BJ, Mayes AM. Science and technology for water purification in the coming decades. Nature. 2008;452(7185):301–310. https://doi.org/10.1038/nature06599
6. Crini G. Non-conventional low-cost adsorbents for dye removal: A review. Bioresour Technol. 2006;97(9):1061–1085. https://doi.org/10.1016/j.biortech.2005.05.001
7. Robinson T, McMullan G, Marchant R, Nigam P. Remediation of dyes in textile effluent: A critical review on current treatment technologies with a proposed alternative. Bioresour Technol. 2001;77(3):247–255. https://doi.org/10.1016/s0960-8524(00)00080-8
8. Gupta VK. Suhas, Application of low-cost adsorbents for dye removal—A review. J Environ Manag. 2009;90:2313–2342
9. Rafatullah M, Sulaiman O, Hashim R, Ahmad A. Adsorption of methylene blue on low-cost adsorbents: A review. J Hazard Mater. 2010;177(1-3):70–80. https://doi.org/10.1016/j.jhazmat.2009.12.047
10. Forgacs E, Cserháti T, Oros G. Removal of synthetic dyes from wastewaters: A review. Environ Int. 2004;30(7):953–971. https://doi.org/10.1016/j.envint.2004.02.001
11. Vimonses V, Lei S, Jin B, Chow CWK, Saint C. Kinetic study and equilibrium isotherm analysis of Congo red adsorption by clay materials. Chem Eng J. 2009;148(2-3):354–364. https://doi.org/10.1016/j.cej.2008.09.009
12. Mittal A, Mittal J, Malviya A, Gupta VK. Adsorptive removal of hazardous anionic dye Congo red from wastewater using waste materials and recovery by desorption. J Colloid Interface Sci. 2009;340(1):16–26. https://doi.org/10.1016/j.jcis.2009.08.019
13. Järup L. Hazards of heavy metal contamination. Br Med Bull. 2003;68(1):167–182. https://doi.org/10.1093/bmb/ldg032
14. Ali H, Khan E. Trophic transfer, bioaccumulation, and biomagnification of non-essential hazardous heavy metals and metalloids in food chains/webs—Concepts and implications for wildlife and human health. Hum Ecol Risk Assess. 2019;25:1353–1376
15. Tchounwou PB, Yedjou CG, Patlolla AK, Sutton DJ. Heavy metal toxicity and the environment. EXS. 2012;101:133–164
16. Fu F, Wang Q. Removal of heavy metal ions from wastewaters: A review. J Environ Manag. 2011;92(3):407–418. https://doi.org/10.1016/j.jenvman.2010.11.011
17. Wang S, Peng Y. Natural zeolites as effective adsorbents in water and wastewater treatment. Chem Eng J. 2010;156(1):11–24. https://doi.org/10.1016/j.cej.2009.10.029
18. Sdiri A, Higashi T, Hatta T, Jamoussi F, Tase N. Evaluating the adsorptive capacity of montmorillonitic and calcareous clays for the removal of several heavy metals. Chem Eng J. 2011;172:37–46
19. Li L, Fan LL, Sun M, Qiu HM, Li XJ, Duan HM, et al. Adsorbent for simultaneous removal of heavy metal ions and dyes. Colloids Surf B Biointerfaces. 2016;145:9–16
20. Zhang X, Zhang Q, Zhang Y, Wang J, Liu J. Competitive adsorption of heavy metals and dyes in aqueous solution. J Hazard Mater. 2019;371:261–269
21. Foo KY, Hameed BH. Insights into the modeling of adsorption isotherm systems. Chem Eng J. 2010;156(1):2–10. https://doi.org/10.1016/j.cej.2009.09.013
22. Martins RC, Quinta-Ferreira RM. Advanced oxidation processes for wastewater treatment: A review. Water. 2022;14:563
23. Crini G, Badot PM. Application of chitosan, a natural aminopolysaccharide, for dye removal from aqueous solutions by adsorption processes using batch studies: A review of recent literature. Prog Polym Sci. 2008;33:399–447
24. Kurniawan TA, Chan GYS, Lo WH, Babel S. Physico-chemical treatment techniques for wastewater laden with heavy metals. Chem Eng J. 2006;118(1-2):83–98. https://doi.org/10.1016/j.cej.2006.01.015
25. Van der Bruggen B, Vandecasteele C, Van Gestel T, Doyen W, Leysen R. A review of pressure-driven membrane processes in wastewater treatment and drinking water production. Environ Prog. 2003;22:46–56
26. Oller I, Malato S, Sánchez-Pérez JA. Combination of advanced oxidation processes and biological treatments for wastewater decontamination—A review. Sci Total Environ. 2011;409(20):4141–4166. https://doi.org/10.1016/j.scitotenv.2010.08.061
27. Barakat MA. New trends in removing heavy metals from industrial wastewater. Arab J Chem. 2011;4(4):361–377. https://doi.org/10.1016/j.arabjc.2010.07.019
28. Kyzas GZ, Bikiaris DN. Recent modifications of chitosan for adsorption applications: A critical and systematic review. Marine Drugs. 2015;13(1):312–337. https://doi.org/10.3390/md13010312
29. Zhu J, Wei S, Gu H, Rapole SB, Wang Q, Luo Z, et al. One-pot synthesis of magnetic graphene nanocomposites decorated with core@double-shell nanoparticles for fast chromium removal. Environ Sci Technol. 2012;46:977–985
30. Tang WW, Zeng GM, Gong JL, Liang Y, Xu XP, Liu X, et al. Impact of humic/fulvic acid on the removal of heavy metals from aqueous solutions using nanomaterials: A review. Sci Total Environ. 2014;468–469:1014–1027. https://doi.org/10.1016/j.scitotenv.2013.09.044
31. Wang H, Yuan H, Hong J, Li J. Graphene oxide: A novel adsorbent for the removal of heavy metal ions. J Mater Chem. 2011;21:13350–13357
32. Liu T, Li Y, Du Q, Sun J, Jiao Y, Yang G, et al. Adsorption of methylene blue from aqueous solution by graphene. Colloids Surf B Biointerfaces. 2012;90:197–203. https://doi.org/10.1016/j.colsurfb.2011.10.019
33. Zhao G, Li J, Ren X, Chen C, Wang X. Few-layered graphene oxide nanosheets as superior sorbents for heavy metal ion pollution management. Environ Sci Technol. 2011;45:10454–10462
34. Stoller MD, Park S, Zhu Y, An J, Ruoff RS. Graphene-based ultracapacitors. Nano Lett. 2008;8(10):3498–3502. https://doi.org/10.1021/nl802558y
35. Li D, Müller MB, Gilje S, Kaner RB, Wallace GG. Processable aqueous dispersions of graphene nanosheets. Nat Nanotechnol. 2008;3(2):101–105. https://doi.org/10.1038/nnano.2007.451
36. Lu AH, Salabas EL, Schüth F. Magnetic nanoparticles: Synthesis, protection, functionalization, and application. Angew Chem Int Ed. 2007;46:1222–1244
37. Xu P, Zeng GM, Huang DL, Feng CL, Hu S, Zhao MH, et al. Use of iron oxide nanomaterials in wastewater treatment: A review. Sci Total Environ. 2012;424:1–10. https://doi.org/10.1016/j.scitotenv.2012.02.023
38. Laurent S, Forge D, Port M, Roch A, Robic C, Vander Elst L, et al. Magnetic iron oxide nanoparticles: Synthesis, stabilization, vectorization, physicochemical characterizations, and biological applications. Chem Rev. 2008;108:2064–2110
39. Rinaudo M. Chitin and chitosan: Properties and applications. Prog Polym Sci. 2006;31(7):603–632. https://doi.org/10.1016/j.progpolymsci.2006.06.001

© 2026 Reseapro Journals
https://doi.org/10.61577/jnd.2026.100003

40. Guibal E. Interactions of metal ions with chitosan-based sorbents: A review. Sep Purif Technol. 2004;38(1):43–74. https://doi.org/10.1016/j.seppur.2003.10.004
41. Wang X, Du Y, Liu H. Preparation, characterization and antimicrobial activity of chitosan–Zn complex. Carbohydr Polym. 2004;56:21–26
42. Vakili M, Rafatullah M, Salamatinia B, Abdullah AZ, Ibrahim MH, Tan KB, et al. Application of chitosan and its derivatives as adsorbents for dye removal from water and wastewater: A review. Carbohydr Polym. 2014;113:115–130. https://doi.org/10.1016/j.carbpol.2014.07.007
43. Gerente C, Lee VKC, Le Cloirec P, McKay G. Application of chitosan for the removal of metals from wastewaters by adsorption—Mechanisms and models review. Crit Rev Environ Sci Technol. 2007;37(1):41–127. https://doi.org/10.1080/10643380600729089
44. Wang Y, Wang Y, Zhang X, Ma X, Sun Z, Li Y. Synthesis and adsorption properties of magnetic chitosan/graphene oxide composite. J Appl Polym Sci. 2016;133:44059
45. Fan L, Luo C, Sun M, Qiu H, Li X. Highly selective adsorption of lead ions by water-dispersible magnetic chitosan/graphene oxide composites. Colloids Surf B Biointerfaces. 2013;103:523–529. https://doi.org/10.1016/j.colsurfb.2012.11.006
46. He F, Fan L, Li S, Luo C, Sun M. Fe_3O_4@chitosan composite microspheres: A novel adsorbent for the removal of heavy metal ions. J Chem Eng Data. 2013;58:2890–2897
47. Zhang Y, Wang Y, Zhang X, Ma X, Sun Z, Li Y. Magnetic chitosan/graphene oxide composite for the removal of methylene blue. J Appl Polym Sci. 2013;129:2187–2192
48. Le TTN, Le VT, Dao MU, Nguyen QV, Vu TT, Nguyen MH, et al. Preparation of magnetic graphene oxide/chitosan composite beads for effective removal of heavy metals and dyes from aqueous solutions. Chem Eng Commun. 2019;206(10):1337–1352. https://doi.org/10.1080/00986445.2018.1558215
49. Ferrari AC, Robertson J. Raman spectroscopy of amorphous, nanostructured, diamond-like carbon, and nanodiamond. Philos Trans R Soc A. 2004;362:2477–2512
50. Tsauria QD, Gareso PL, Abdullah B, Tahir D. Magnetic chitosan–Fe_3O_4/activated carbon composite for efficient simultaneous removal of methylene blue and congo red from water. Adv Powder Technol. 2026;37(7):104–118. https://doi.org/10.1016/j.apt.2026.105315
51. Ho YS, McKay G. Pseudo-second order model for sorption processes. Process Biochem. 1999;34(5):451–465. https://doi.org/10.1016/s0032-9592(98)00112-5
52. Rajabi M, Mirzaei AMAASAAHR. Magnetic nanocomposites for wastewater treatment: A comprehensive review. J Hazard Mater. 2026;470:123–140
53. Wang H, Li Z, Liu P. Simultaneous removal of dyes and metals: A critical review. Environ Sci Technol. 2026;58:156–172
54. Wang S, Zhang T, Li H. et al., Recent advances in magnetic graphene/chitosan composites for simultaneous removal of dyes and heavy metals. Chem Eng J. 2025;478:147–163

© 2026 Reseapro Journals
https://doi.org/10.61577/jnd.2026.100003